Journal of Materials Chemistry A

PAPER

View Article Online
View Journal

Cite this: DOI: 10.1039/c8ta10738f

Design of an amorphous TaO_x multifunctional interfacial layer on photocathodes for photoelectrochemical H_2 evolution†

Sang Youn Chae, [a] Sumin Kim[b] and Oh-Shim Joo *[a]

A novel TaO_x multifunctional layer which is transparent and co-catalytically active was applied to photoelectrodes for hydrogen production. We found that amorphous TaO_x was *in situ* transformed into amorphous $TaO_x/Ta(OH)_x$ in the photoelectrochemical reaction, which is a more active form for hydrogen evolution. The $TaO_x/Ta(OH)_x$ multifunctional layer enhanced not only charge separation but also stability and HER kinetics when it was deposited on a p-type $CuInS_2$ model photocathode. The new band alignment and the widened depletion region of $CuInS_2/TaO_x$ were revealed by electrochemical impedance spectroscopy and IPCE analysis. The TaO_x deposited $CuInS_2$ photocathode shows a higher photocurrent at −0.3 V *vs.* RHE compared to $CuInS_2$ or even Pt-decorated $CuInS_2$. A novel multifunctional layer was successfully designed and demonstrated for photocathodes without noble metals, which can minimize the structure of photoelectrodes.

Received 7th November 2018
Accepted 18th December 2018

DOI: 10.1039/c8ta10738f

rsc.li/materials-a

Introduction

The photoelectrochemical (PEC) cell for hydrogen production has been intensively researched because the conversion of solar energy to hydrogen is deemed to be one of the methods for alternative renewable energy storage since Fujishima–Honda's result.[1] One of the key factors for the photoelectrochemical reaction is the semiconductor–liquid junction (SLJ) at the interface between photoelectrodes and electrolytes. There are various strategies to enhance the interface properties of semiconductors, for instance, doping,[2–4] passive layer formation,[5–7] heterojunction,[8,9] and embedding of a p–n junction structure.[10]

Among the various methods, the passivation of semiconductor surfaces is one of the important strategies for efficient charge carrier separation. The improvement of interface properties in the SLJ is critical to obtain high PEC activity since the driving force of photoelectrochemical reactions originates from the interface properties. Charge recombination at surface states is one of the main obstacles, which can be suppressed by applying a passive layer on semiconductor surfaces. A wide band gap material that has a low valence band maximum is usually used for the passive layer. In that case, the drift of a hole toward back recombination would be difficult due to cascade valence band energy levels.[5] In addition, the stability issue of photoelectrodes is another key factor for practical implementation. Surface passivation can also increase the stability of photoelectrodes[11–13] because the passive layer may block the corrosion reaction paths of semiconductors.

Another important aspect of the SLJ is the presence of electrochemical reactions between semiconductors and electrolytes. When the conduction band of a semiconductor is higher enough than the redox potential of the hydrogen evolution reaction (HER), the photoelectrode can produce hydrogen under light illumination conditions. However, most of the semiconductors show poor photoelectrochemical activity due to the high overpotential of the HER without a co-catalyst.[14] It is clear that enhancing the kinetics of the HER is also as important as the improvement of semiconductors in terms of bulk and interface properties. For example, the deposition of Pt on semiconductors shows great improvement in HER activities.

Therefore, most photocathodes are designed as the structure of multiple composites with a semiconductor, a passive layer, and a co-catalyst. However, the multilayer structure generates more interfaces between each component, and the preparation process would be complicated. Unlike electrochemical reactions, charge carrier transport at the interfaces can be a bottleneck of photoelectrochemical reactions. The multi-layer structure might show the advantages of each component, however, it might also indicate the drawbacks in the interfaces. The importance of interfacial contacts between co-catalysts and passive layers or passive layers and semiconductors has been pointed out by our and other groups.[15–18]

Therefore, we have designed a multifunctional layer for photocathodes to minimize interface formation between contacts. To be an ideal interface layer, both HER activities and

[a]*Clean Energy Research Center, Korea Institute of Science and Technology, Seoul 02792, Republic of Korea. E-mail: joocat@kist.re.kr*

[b]*Department of Chemical Engineering, Pohang University of Science and Technology, Pohang 37673, Republic of Korea*

† Electronic supplementary information (ESI) available. See DOI: 10.1039/c8ta10738f

charge transport properties should be satisfied with good electrochemical stability. Furthermore, the interfacial layer should have the least of light absorption. However, it is hard to find an ideal candidate material for the multi-functional interface layer. Most of the good electrocatalysts have high light absorption properties and reflection, and most of the passive layers have poor HER catalytic behavior.

We have paid attention to amorphous metal oxides to design a multifunctional layer for semiconductors. Wide band gap metal oxides have excellent properties for photoelectrochemical reactions, for example, low light absorption, passivation ability, and good stability. Improvement of HER activities has been reported for some metal oxides/oxyhydroxides or hydroxide mixtures,[19–22] even though metal oxides have generally shown relatively poor HER activities. For example, the very surface of a ruthenium oxide layer could be transformed into the ruthenium hydroxide form under reductive electrochemical conditions, and thus the HER activity was significantly increased.[23]

In this article, we introduce a multifunctional amorphous tantalum oxide layer into the photocathode of p-type $CuInS_2$, which improves the stability, charge separation, and HER activity of semiconductors. The deposited amorphous tantalum oxide showed good suppression of charge recombination when it was applied to the $CuInS_2$ surface. And the HER activity was improved with the transformation of TaO_x to $Ta(OH)_x$ during the photoelectrochemical reaction. In this case, the $TaO_x/Ta(OH)_x$ layer successfully passivates surface states and boosts the HER activity in the $CuInS_2$ photocathode. As a result, $CuInS_2/TaO_x/Ta(OH)_x$ shows higher photo-activities and photo-stabilities than a $CuInS_2$/Pt photocathode at a more negative potential than 0.0 V *vs.* RHE. This concept of a novel and versatile layer could be useful to design an ideal interfacial layer for photoelectrodes.

Experimental

$CuInS_2$ film preparation

$CuInS_2$ was grown on a 500 nm Mo-coated soda-lime glass by an electrodeposition–sulfurization method. The copper layer was deposited at −0.4 V *vs.* Ag/AgCl applied potential in a 10 mM $CuSO_4 \cdot 5H_2O$ (Kanto Chemical Co., Inc., 99%) and 10 mM citric acid (Sigma-Aldrich, 99.5%) electrolytic bath for 1650 s. The indium layer was consecutively deposited at −0.78 V *vs.* Ag/AgCl applied potential in a 30 mM $InCl_3 \cdot 4H_2O$ (Sigma-Aldrich, 99.999%), 10 mM citric acid (Sigma-Aldrich, 99.5%), and 36 mM sodium citrate (Sigma-Aldrich, 99.9%) electrolytic bath for 1780 s. The Cu–In film was annealed in a tube furnace at 110 °C for 1 h, and then 520 °C for 10 min in a N_2 atmosphere, subsequently 520 °C for 40 min in a 1% H_2S (N_2 balance) atmosphere. After annealing, the $CuInS_2$ film was dipped in 0.1 M KCN (Sigma-Aldrich, 98%) for 1 min and 28% NH_4OH (Junsei, 28%) for 10 min to etch the remaining binary phases of Cu or In after the sulfurization.

Amorphous TaO_x and Pt deposition on $CuInS_2$

An amorphous TaO_x layer (30 nm thickness) was deposited on a $CuInS_2$ film or a glassy carbon using an e-beam evaporator (KVE-E2006, Korea vacuum tech) with a Ta_2O_5 source (LTS Research Laboratories, Inc., 99.995%). $CuInS_2/TaO_x$ was annealed in a tube furnace at 200 °C for 2 h in a 1% H_2S (N_2 balance) atmosphere. Platinum was also deposited on a $CuInS_2$ film by an electrodeposition method at −0.1 V *vs.* Ag/AgCl applied potential in a 1 mM $H_2PtCl_6 \cdot 6H_2O$ (Sigma-Aldrich, ≥37.50% Pt basis) electrolytic bath for 120 s. The deposition time of Pt was optimized for the best photoelectrochemical activity.

Photoelectrochemical characterization

Linear sweep voltammetry (LSV, 10 mV s^{-1} scan rate) and chronoamperometry (at −0.5 V *vs.* Ag/AgCl) were performed with a potentiostat (Ivium, IviumStat) with a conventional three-electrode system to characterize photoelectrochemical activity and stability. The counter and reference electrodes were a graphite rod and Ag/AgCl (3 M NaCl). The electrolyte was a 0.5 M H_2SO_4 (Sigma-Aldrich, 95–98%) aqueous solution (pH 0.35–0.39). The applied potential ($E_{Ag/AgCl}$) was converted to the potential *versus* the reversible hydrogen electrode (E_{RHE}) using eqn (1).

$$E_{RHE}\,(V) = E_{Ag/AgCl}\,(V) + 0.0591pH + 0.209\ V \quad (1)$$

Illumination light was simulated as sunlight with 1 sun intensity (100 mW cm^{-2}) using a solar simulator (ABET, Sun 2000) equipped with an AM 1.5 filter.

To measure the flat band potential of photoelectrodes, Mott–Schottky analysis was carried out in a 1000 Hz frequency range at 0.7 to 1.2 V *vs.* Ag/AgCl applied potential. Electrochemical impedance spectroscopy was performed within the frequency range of 10^6 to 0.1 Hz at 0.0 to −0.4 V *vs.* Ag/AgCl applied potential. The data was fitted using Z view software. The incident photon to current conversion efficiency (IPCE) of photoelectrodes was measured at 0.0 V *vs.* RHE using a Xe lamp of 1000 W with a cut-off filter of 400 and 600 nm equipped with a monochromator (Newport, cornerstone 1/4).

Faradaic efficiency measurement

To measure the faradaic efficiency of photoelectrochemical reactions on photocathodes, chronoamperometry was carried out on $CuInS_2/TaO_x$ photocathodes at −0.3 V *vs.* Ag/AgCl applied potential in an electrochemical cell equipped with a closed quartz window.

Evolved H_2 gas was directly injected into an online gas chromatograph (Yonglin, YL6500) equipped with a molecular sieve 13X column, a flame induced detector (FID), and a thermal conductivity detector (TCD) during the photoelectrochemical reaction. The faradaic efficiency was calculated using eqn (2) and (3),

$$I_{H_2} = (\phi_{H_2}) \times Q \times \frac{2Fp}{RT} \quad (2)$$

$$\eta_F = \frac{I_{H_2}}{I} \times 100\% \quad (3)$$

where I_{H_2} is the current of H_2 evolution, ϕ_{H_2} is the volume concentration of H_2, Q is the injected gas volumetric flow rate (100 mL min^{-1}), F is the Faraday constant, p is the atmosphere pressure, T is the temperature of the electrochemical cell, R is the ideal gas constant, η_F is the faradaic efficiency, and I is the steady-state photocurrent.

Material characterization

The surface morphology and atomic ratio of photoelectrodes were investigated by scanning electron microscopy (SEM, Hitachi, S-4200 and FEI, Inspect F) and energy dispersive X-ray spectroscopy (FEI, Inspect F). A transmission electron microscope (TEM, FEI, Tecnai F20 G2) was used to investigate the cross-sectional structure of $CuInS_2/TaO_x$ films. The cross-sectional ablation of $CuInS_2/TaO_x$ was carried out using a focused ion beam. A topological analysis was carried out using an atomic force microscope (AFM, Park systems, XE-100). Light absorbance properties were analysed using an UV-VIS-NIR spectrometer (Agilent, Cary-5000). Crystallography was also performed by X-ray diffraction (XRD) using an X-ray diffractometer (Shimadzu, XRD-6000 and Rigaku and D'Max 2500/PC). X-ray photoelectron spectroscopy (XPS) and ultraviolet spectroscopy (UPS) were carried out using an XPS analysis system (Ulvac-PHI, PHI 5000 VersaProbe). Time of flight secondary ion mass spectroscopy (TOF-SIMS) was carried out using a TOF-SIMS instrument (IONTOF, TOF.SIMS 5). Rutherford backscattering spectroscopy (RBS) was used to characterize atomic compositions in the accelerator center of KIST (Korea Institute of Science and Technology).

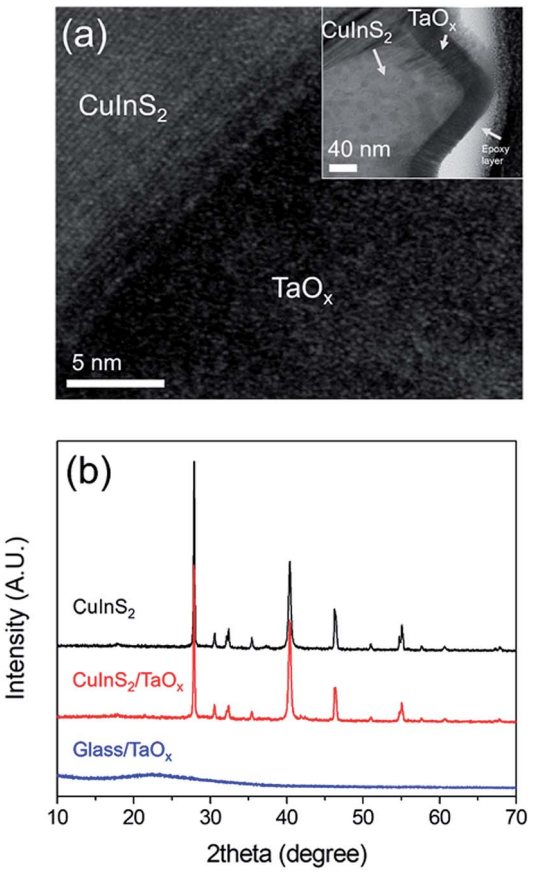

Fig. 1 (a) Cross-sectional TEM images of $CuInS_2/TaO_x$. (b) XRD results of $CuInS_2$, $CuInS_2/TaO_x$, and glass/TaO_x.

Results and discussion

The amorphous phase of TaO_x was obtained by e-beam deposition on the $CuInS_2$ surface due to the desublimation of the TaO_x precursor vapor on the substrate without additional crystal formation energy. After TaO_x was coated on $CuInS_2$, heat treatment was carried out at a mild temperature (200 °C). The heat treatment does not affect the crystal phase of the tantalum oxide, $CuInS_2$, or substrates. HR-TEM images and XRD results (Fig. 1) show the amorphous nature of TaO_x films, and therefore, further 'TaO_x' indicates the amorphous phase of tantalum oxide. The shifted binding energy of tantalum was observed by XPS analysis, which indicates that TaO_x reduced slightly after heat treatment (Fig. S1(a),† 'as deposited' and 'as annealed' which mean the TaO_x as-deposited and heat-treated, respectively). The oxygen was also fitted as an oxide[24] and an adsorbed H_2O,[25] but the H_2O peak was eliminated and a new peak arose after heat treatment. The new peak was concluded as hydroxides by SIMS data, which will be further discussed (Fig. S1(b),† as deposited and as prepared).

Then, the electrochemical/photoelectrochemical activities of $CuInS_2$ photocathodes with a Pt co-catalyst or TaO_x coating were characterized. To be a multifunctional interfacial layer, TaO_x layers should show HER activity. Therefore, the electrochemical activity of TaO_x deposited on a glassy carbon was also measured for the HER. TaO_x shows poor initial HER activity, but the HER activity was increased and saturated by the repeated scanning of LSV (Fig. 2a). The overpotential at 10 mA cm^{-2} was significantly improved to 847 mV after the saturation. Similar behavior was observed when TaO_x was deposited on $CuInS_2$, and the photocurrent was also increased and saturated by several LSV scans (Fig. 2b).

This 'activated' (which means TaO_x samples after the repeated scanning of LSV) $CuInS_2/TaO_x$ photocathode shows excellent activity compared to bare $CuInS_2$, and it can be comparable to even noble metal Pt-decorated $CuInS_2$ (Fig. 2c). Tafel slopes were estimated from the LSV results (Fig. 2d), and the J–V graph shows a non-logarithmic dependency on the potential due to photo-carrier recombination processes.[21] The onset potential was determined by the Tafel slope for each photocathode at 0.1, 0.2, and 0.25 V *vs.* RHE for $CuInS_2$, $CuInS_2/TaO_x$, and $CuInS_2$/Pt, respectively.

TaO_x showed an additional onset potential of only 50 mV compared to Pt, when it was combined with $CuInS_2$. This good activity of TaO_x might originate from not only HER kinetics but also charge recombination suppression from the passivation effect. The Tafel slopes of $CuInS_2/TaO_x$ and $CuInS_2$/Pt show the values of 45.2 and 74.5 mV dec^{-1}. Usually, Tafel slopes indicate electrochemical kinetics, but it may not be valid for photoelectrochemical reactions because both photo-induced charge recombination and electrochemical kinetics have to be

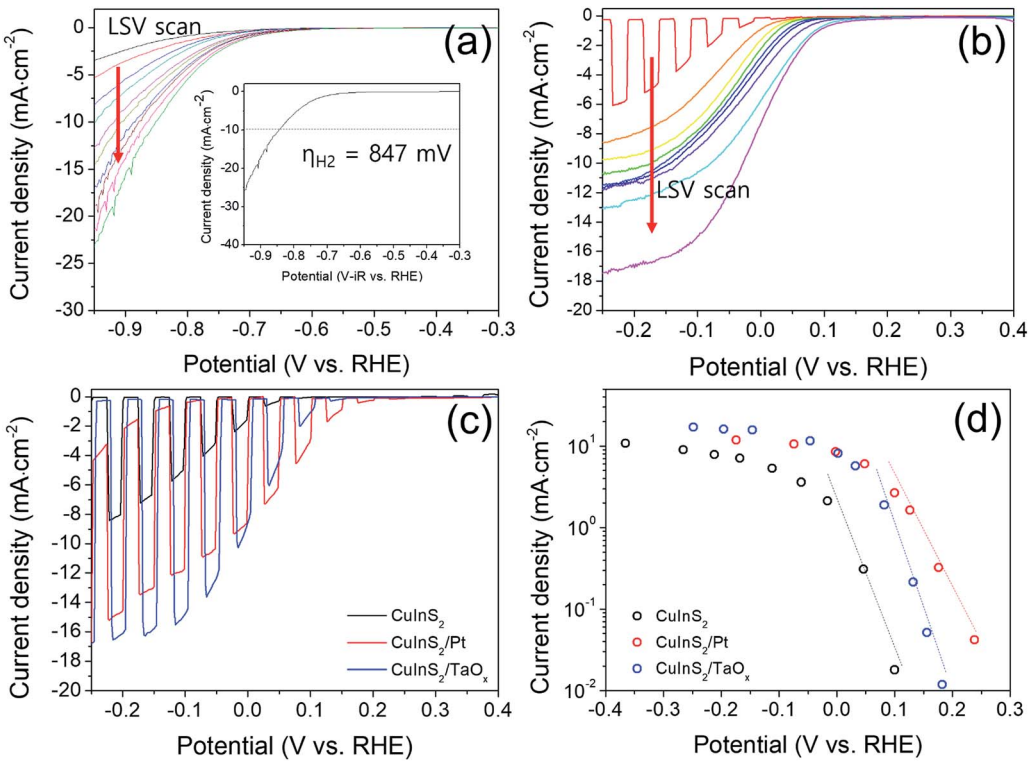

Fig. 2 LSV results of (a) TaO_x deposited on a glassy carbon and (b) $CuInS_2/TaO_x$. (c) Photocurrent comparison of bare $CuInS_2$, $CuInS_2$/Pt, and $CuInS_2/TaO_x$. (d) Tafel slopes of photocurrent.

considered in the reactions.[26] Therefore, detailed characterization has been carried out to confirm the multifunctional effects of TaO_x on co-catalytic HER activity and passivation.

Firstly, the chemical composition was examined to figure out the increased HER activity on the $CuInS_2/TaO_x$. TOF-SIMS analysis indicates that the $CuInS_2/TaO_x$ 'as-prepared' and 'activated' shows different hydrogen profiles by depth (Fig. 3a). It is noted that the distribution of Ta, O, and H in the depth profile is different from the real thickness (~30 nm) due to the high roughness of $CuInS_2$ (~ 280 nm, see SEM and AFM results in Fig. S2; † also SEM images and EDS results of $CuInS_2$, $CuInS_2$/Pt, and $CuInS_2/TaO_x$ in Fig. S3 and S4, and Table S1†).

The relative hydrogen atom ratio was increased by the activation process (the repeated scanning of LSV). From the exact atomic ratio of the entire TaO_x layer revealed by RBS results, it is found that the ratio of Ta to O is 1.4 : 5, regardless of the as-prepared or activated samples (Fig. 3(b)). The XPS O 1s result shows two deconvoluted peaks, one originates from tantalum oxide,[24] and the origin of the other peak is unknown. However, the SIMS results pointed out that the number of the hydrogen atoms increased and the XPS results showed that the binding energy of Ta 4f (TaO_x) reduced after the electrochemical activation step. Therefore, we conclude that the unknown peak indicates hydroxide states due to the formation of tantalum hydroxide under reductive conditions (Fig. 3(c)). It is reported that metal oxides are converted to the metal hydroxides under electrochemical reductive conditions,[19,21,27] and part of the metal hydroxides or metal oxyhydroxides ($Ru(OH)_x$, NiO_x, NiFeOOH) show better HER activities than their oxide forms.[19–23] Therefore, the *in situ* transformation into

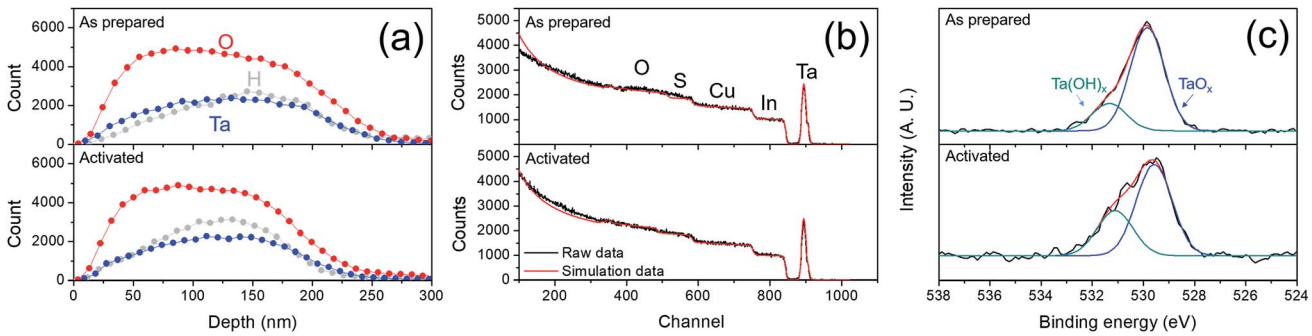

Fig. 3 Analysis of as prepared and activated (after the repeated scanning of LSV) $CuInS_2/TaO_x$ using (a) SIMS, (b) RBS, and (c) XPS O 1s spectra.

$Ta(OH)_x$ could be critical for the improved HER activities on a TaO_x layer.

Meanwhile, the suppression of charge recombination on $CuInS_2/TaO_x$ and $CuInS_2$/Pt was also investigated by electrochemical analysis. EIS (electrochemical impedance spectroscopy) was carried out for $CuInS_2$/Pt and $CuInS_2/TaO_x$, and the results were fitted using an equivalent circuit in Fig. 4 (the detailed Nyquist plots and Bode plots are shown in Fig. S5†). R_{sol} is the solution resistance, R_{bulk} and CPE_{bulk} are the charge transfer resistance and the constant phase element in the bulk of semiconductors, and $R_{surface}$ and $CPE_{surface}$ are the charge transfer resistance and the constant phase element *via* charge trapping in surface states. Interestingly, the $R_{surface}$ value dramatically decreased when TaO_x was deposited on $CuInS_2$, while the R_{bulk} values were similar for both $CuInS_2/TaO_x$ and $CuInS_2$/Pt. The small R_{surf} indicates that charge carrier transportation is easier due to less chance of charge trapping by the TaO_x passivation layer.[28–30] The lifetime of charge carriers ($\tau_{surface}$) at surface states was also calculated by the equation $\tau_{surface} = CPE_{surface} \times R_{bulk}$,[30] and $CuInS_2/TaO_x$ shows ~10–100 times longer lifetime than $CuInS_2$/Pt ($CPE_{surface}$ is shown in Fig. S6†). Therefore, the Pt catalyst mainly affects HER kinetics, not suppressing charge recombination at surface states.

In addition, the thickness of passive layers is important. To investigate the charge transfer behavior of TaO_x, the thickness of TaO_x was controlled to be 15, 30, and 100 nm. The activity of the samples is shown in Fig. S7(a)†. The photocurrent and onset potential of $CuInS_2/TaO_x$ coated by 15 nm or 100 nm TaO_x were inferior to those of $CuInS_2/TaO_x$ coated by 30 nm TaO_x. Thus, EIS was carried out for $CuInS_2/TaO_x$ samples with the difference in thickness to investigate charge transfer (Fig. S7(b) and Table S2†), and it was found that $R_{surface}$ is much higher in the thick passive layer. The high $R_{surface}$ can also affect R_{bulk}, because $R_{surface}$ limits the overall charge transfer process of the photocathode. On the other hand, in the case of the thinner passive layer, charge transfer at the surface is not a problem. Both $R_{surface}$ and R_{bulk} values of the 15 nm sample were similar to those of the 30 nm sample. However, the CPE value of the 15 nm sample was quite lower than that of the 30 nm sample. It would mean that the dissimilar structure in band bending leads to the different photoactivity. Therefore, we analysed the effect of TaO_x on the band bending structure.

The passivation layer of TaO_x also affected the band banding structure of $CuInS_2$, as confirmed by the Mott–Schottky analysis (Fig. 5a). The charge carrier density was very similar with/without TaO_x, but the shifting of the flat band potential was observed. The flat band potential shift might be due to the equilibration of Fermi levels among the $CuInS_2/TaO_x$/electrolyte. From the UV-vis spectra, Mott–Schottky plots, and UPS results of $CuInS_2$ and TaO_x (Fig. S8†), band alignment was suggested as shown in Fig. 5b. The band gap of $CuInS_2$ was obtained as 1.45 eV from the absorbance spectrum, which corresponded to the values in the literature.[31–33] The band gap of crystalline tantalum oxide was 3–5 eV by the stoichiometry.[34–36] In our case, $Ta_{1.4}O_{5\text{-}x}$ shows a band gap of 3.15 eV. The depletion width (w_d) at 0.0 V *vs.* RHE was also calculated using eqn (4),[37]

$$w_d = \left[\left(\frac{2\varepsilon_o\varepsilon_r}{eN_D}\right)\left(V - V_{fb} - \frac{k_B T}{e}\right)\right]^{\frac{1}{2}} \quad (4)$$

where ε_o is the vacuum permittivity, ε_r is the dielectric constant of $CuInS_2$,[38] e is an elementary charge, N_D is the donor density, V is the applied potential, V_{fb} is the flat band potential, k_B is the Boltzmann constant, and T is the temperature. The calculated depletion width of $CuInS_2$ was ~55.94 nm, but it increased to ~63.37 nm when TaO_x was deposited on the $CuInS_2$ surface. A longer depletion width allows efficient charge carrier transportation because only photo-excited charge carriers within effective thickness (diffusion length (D_L) + depletion width (w_d)) can contribute to PEC reactions.[39]

This corresponds to IPCE results in Fig. 5d. The IPCE was measured at 0.0 V *vs.* RHE (the potential which is both $CuInS_2$/Pt and $CuInS_2/TaO_x$ show very similar photocurrent density value), and the IPCE values of $CuInS_2/TaO_x$ were observed to increase at 650–800 nm. The longer wavelength light is absorbed in the deeper depth of the semiconductor than the shorter wavelength light due to its longer penetration depth (low absorption coefficient), and then most of the minority carriers which are excited by the longer wavelength light have to be transported to depletion regions *via* longer distances (Fig. 5(c)).[40] Since TaO_x deposition increased the depletion region, the photo-charge carriers could be easily transported to the depletion region with less recombination chance. On the other hand, the IPCE value of $CuInS_2/TaO_x$ decreased at a short wavelength of 300–500 nm compared to $CuInS_2$/Pt, and this might be because of the light absorption of the TaO_x film (Fig. S8(b)†). Therefore, the TaO_x layer contributes not only to the HER catalytic activity of $CuInS_2$ but also to the suppression

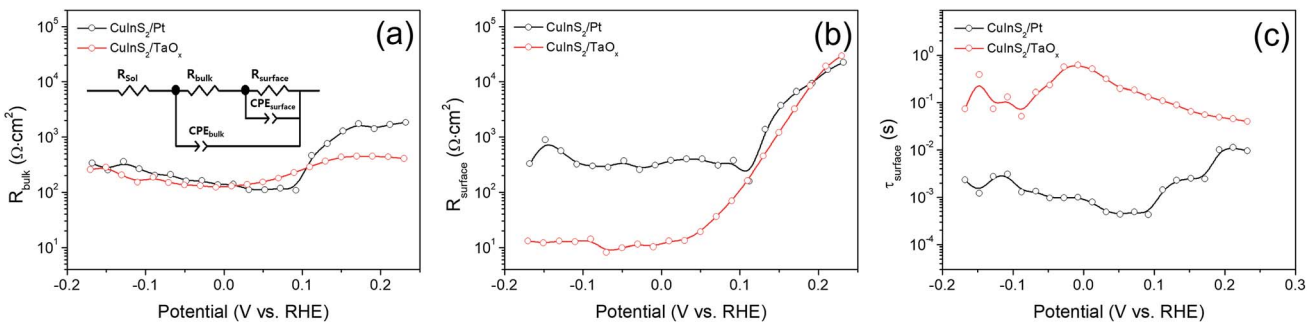

Fig. 4 Comparison of $CuInS_2$/Pt to $CuInS_2/TaO_x$ (a) R_{bulk}, (b) $R_{surface}$, and (c) lifetime of electrons in the semiconductor surface region ($\tau_{surface}$).

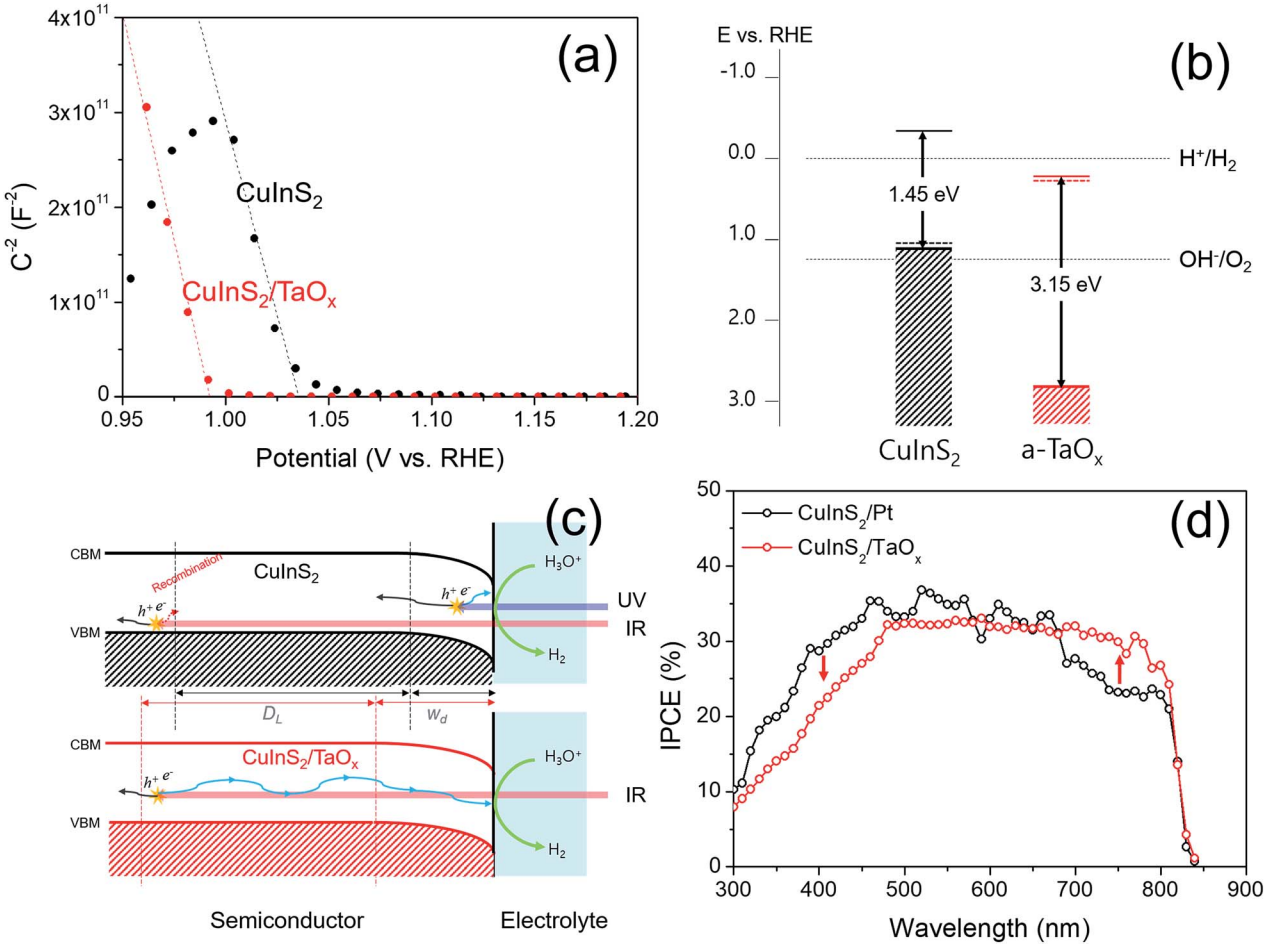

Fig. 5 (a) Mott–Schottky plots of $CuInS_2$ and $CuInS_2/TaO_x$ (b) band positions of $CuInS_2$ and TaO_x (c) a schematic diagram of band bending of $CuInS_2$ photoelectrodes. The depletion width (w_d) is widened with TaO_x deposition, while the diffusion length of electrons (D_L) is independent of TaO_x deposition. (d) IPCE results of $CuInS_2$/Pt and $CuInS_2/TaO_x$.

of charge recombination due to the longer depletion width and passivation of surface states.

Lastly, a stability test was carried out for $CuInS_2$, $CuInS_2$/Pt, and $CuInS_2/TaO_x$. The activity of $CuInS_2$/Pt decreased to ~30% after 2 h, while the initial performance of ~80% was sustained for the $CuInS_2/TaO_x$ photocathode for 3 h (Fig. S9†). This instability might come from the degradation of $CuInS_2$. Even though TaO_x was fully covered on the $CuInS_2$ surface, cracks were found on the TaO_x layer (Fig. S3 (d)†). Therefore, the acidic electrolyte could come into contact with $CuInS_2$, and photo- or electro-degradation reactions on $CuInS_2$ could occur. In addition, an average faradaic efficiency of 93.3% was obtained from the $CuInS_2/TaO_x$ photocathode for 2 h, and then most of the electrons were used in the HER. The deviation of the faradaic efficiency from 100% is due to degradation reactions, and the bubble coalescence of H_2 gas at the electrode surface (Fig. S10†).

In summary, amorphous TaO_x was demonstrated for a multifunctional interfacial layer which has the ability for surface passivation, electrochemical catalytic activity, and stability. The enhanced HER activity originates from the *in situ* transformation of TaO_x into $Ta(OH)_x$ during LSV scanning. In this study, a multifunctional layer was applied to $CuInS_2$ as a model photocathode, and increased photoelectrochemical activity was observed even without a noble metal co-catalyst. There are many chances to improve the electrochemical HER activity of TaO_x, and it might be achieved by doping or alloying with other transition metals. This novel concept of the multifunctional layer can be a milestone for more efficient and simplified structures and photoelectrode materials.

Conflicts of interest

There are no conflicts to declare.

Acknowledgements

This study was supported by the institutional program of the Korea Institute of Science and Technology (KIST).

Notes and references

1 A. Fujishima and K. Honda, *Nature*, 1972, **238**, 37.
2 F. F. Abdi, L. Han, A. H. M. Smets, M. Zeman, B. Dam and R. van de Krol, *Nat. Commun.*, 2013, **4**, 2195.

3 Y.-S. Hu, A. Kleiman-Shwarsctein, A. J. Forman, D. Hazen, J.-N. Park and E. W. McFarland, *Chem. Mater.*, 2008, **20**, 3803–3805.
4 X. Feng, R. Li, M. Wang and Y. Chen, *J. Mater. Chem. A*, 2018, **6**, 11180–11188.
5 R. Liu, Z. Zheng, J. Spurgeon and X. Yang, *Energy Environ. Sci.*, 2014, **7**, 2504–2517.
6 I. A. Moreno-Hernandez, B. S. Brunschwig and N. S. Lewis, *Adv. Energy Mater.*, 2018, **8**, 1801155.
7 A. C. Nielander, A. C. Thompson, C. W. Roske, J. A. Maslyn, Y. Hao, N. T. Plymale, J. Hone and N. S. Lewis, *Nano Lett.*, 2016, **16**, 4082–4086.
8 P. Zhang, L. Yu and X. W. Lou, *Angew. Chem., Int. Ed.*, 2018, **57**, 15076–15080.
9 P. Zhang, B. Y. Guan, L. Yu and X. W. Lou, *Chem*, 2018, **4**, 162–173.
10 S. W. Boettcher, E. L. Warren, M. C. Putnam, E. A. Santori, D. Turner-Evans, M. D. Kelzenberg, M. G. Walter, J. R. McKone, B. S. Brunschwig, H. A. Atwater and N. S. Lewis, *J. Am. Chem. Soc.*, 2011, **133**, 1216–1219.
11 Y. W. Chen, J. D. Prange, S. Dühnen, Y. Park, M. Gunji, C. E. D. Chidsey and P. C. McIntyre, *Nat. Mater.*, 2011, **10**, 539.
12 A. Paracchino, V. Laporte, K. Sivula, M. Grätzel and E. Thimsen, *Nat. Mater.*, 2011, **10**, 456.
13 M. H. Lee, K. Takei, J. Zhang, R. Kapadia, M. Zheng, Y.-Z. Chen, J. Nah, T. S. Matthews, Y.-L. Chueh, J. W. Ager and A. Javey, *Angew. Chem., Int. Ed.*, 2012, **51**, 10760–10764.
14 J. E. Thorne, Y. Zhao, D. He, S. Fan, S. Vanka, Z. Mi and D. Wang, *Phys. Chem. Chem. Phys.*, 2017, **19**, 29653–29659.
15 F. Lin and S. W. Boettcher, *Nat. Mater.*, 2013, **13**, 81.
16 S. Y. Chae, C. S. Lee, H. Jung, O.-S. Joo, B. K. Min, J. H. Kim and Y. J. Hwang, *ACS Appl. Mater. Interfaces*, 2017, **9**, 19780–19790.
17 T. W. Kim and K.-S. Choi, *Science*, 2014, **343**, 990–994.
18 Y. He, J. E. Thorne, C. H. Wu, P. Ma, C. Du, Q. Dong, J. Guo and D. Wang, *Chem*, 2016, **1**, 640–655.
19 Y. Sugawara, A. P. Yadav, A. Nishikata and T. Tsuru, *J. Electrochem. Soc.*, 2008, **155**, B897–B902.
20 X. Yu, J. Zhao, L.-R. Zheng, Y. Tong, M. Zhang, G. Xu, C. Li, J. Ma and G. Shi, *ACS Energy Lett.*, 2018, **3**, 237–244.
21 E. Pastor, F. Le Formal, M. T. Mayer, S. D. Tilley, L. Francàs, C. A. Mesa, M. Grätzel and J. R. Durrant, *Nat. Commun.*, 2017, **8**, 14280.
22 J. Luo, J.-H. Im, M. T. Mayer, M. Schreier, M. K. Nazeeruddin, N.-G. Park, S. D. Tilley, H. J. Fan and M. Grätzel, *Science*, 2014, **345**, 1593–1596.
23 H. Kaneko, T. Minegishi, T. Higashi, M. Nakabayashi, N. Shibata and K. Domen, *Small Methods*, 2018, **2**, 1800018.
24 J. H. Thomas and L. H. Hammer, *J. Electrochem. Soc.*, 1989, **136**, 2004–2010.
25 N. Mårtensson, *Molecular and Solid Water – a Comparative ESCA Study*, Inst. of Physics, Univ., 1976.
26 A. M. Fajardo and N. S. Lewis, *J. Phys. Chem. B*, 1997, **101**, 11136–11151.
27 J. Juodkazytė, R. Vilkauskaitė, B. Šebeka and K. Juodkazis, *Trans. IMF*, 2007, **85**, 194–201.
28 B. Eftekharinia, A. Moshaii, A. Dabirian and N. S. Vayghan, *J. Mater. Chem. A*, 2017, **5**, 3412–3424.
29 B. Klahr, S. Gimenez, F. Fabregat-Santiago, J. Bisquert and T. W. Hamann, *J. Am. Chem. Soc.*, 2012, **134**, 16693–16700.
30 M. S. Prévot, X. A. Jeanbourquin, W. S. Bourée, F. Abdi, D. Friedrich, R. van de Krol, N. Guijarro, F. Le Formal and K. Sivula, *Chem. Mater.*, 2017, **29**, 4952–4962.
31 R. Scheer, *Prog. Photovoltaics*, 2012, **20**, 507–511.
32 M. B. Rabeh, N. Khedmi, M. A. Fodha and M. Kanzari, *Energy Procedia*, 2014, **44**, 52–60.
33 J. L. Shay, B. Tell, H. M. Kasper and L. M. Schiavone, *Phys. Rev. B: Condens. Matter Mater. Phys.*, 1972, **5**, 5003–5005.
34 K. Kukli, J. Aarik, A. Aidla, O. Kohan, T. Uustare and V. Sammelselg, *Thin Solid Films*, 1995, **260**, 135–142.
35 R. Nashed, W. M. I. Hassan, Y. Ismail and N. K. Allam, *Phys. Chem. Chem. Phys.*, 2013, **15**, 1352–1357.
36 R. M. Fleming, D. V. Lang, C. D. W. Jones, M. L. Steigerwald, D. W. Murphy, G. B. Alers, Y.-H. Wong, R. B. v. Dover, J. R. Kwo and A. M. Sergent, *J. Appl. Phys.*, 2000, **88**, 850–862.
37 N. Mirbagheri, D. Wang, C. Peng, J. Wang, Q. Huang, C. Fan and E. E. Ferapontova, *ACS Catal.*, 2014, **4**, 2006–2015.
38 A. Kotbi, A. Ridah, B. Hartiti and P. Thevenin, *The optical parameters of $CuInS_2$ thin films deposited by spray pyrolysis method for photovoltaic applications, 2015 3rd International Renewable and Sustainable Energy Conference (IRSEC)*, Marrakech, 2015, pp. 1–4. DOI: 10.1109/IRSEC.2015.7455125.
39 W. W. Gärtner, *Phys. Rev.*, 1959, **116**, 84–87.
40 S. Y. Chae, S. J. Park, S. G. Han, H. Jung, C.-W. Kim, C. Jeong, O.-S. Joo, B. K. Min and Y. J. Hwang, *J. Am. Chem. Soc.*, 2016, **138**, 15673–15681.